ORIGINAL PAPER

Touraj Farsadi · Davood Asadi · Hasan Kurtaran

Nonlinear flutter response of a composite plate applying curvilinear fiber paths

Abstract In the present study, nonlinear flutter and post-flutter behavior of a variable stiffness composite wing-like plate is investigated. The variable stiffness is obtained by varying fiber angles continuously according to a selected curvilinear fiber path function in the composite laminates. Flutter speed, limit cycle oscillations and bifurcation diagrams of the composite plate are explored for three different fiber path functions using the nonlinear structural model obtained based on the virtual work principle. The paper aims to exploit the ideal fiber paths with enhanced aeroelastic flutter and post-flutter properties for a composite plate in supersonic flow speed. First-order linear piston theory is applied to model the aerodynamics, and generalized differential quadrature is employed to solve the governing equations. Von Karman nonlinear strain theory is used to account for the geometric nonlinearities, and first-order shear deformation theory is employed to consider the transverse shear effects in the structural model. Time integration of the equation of motion is carried out using the Newmark average acceleration method. Different curvilinear fiber paths are introduced to enhance flutter instabilities and post-flutter behavior of the composite plate. Results demonstrate that the fiber orientation has a significant effect on the dynamic behavior of the plate and the asymmetric properties as well as the behavior of the limit cycle oscillation.

1 Introduction

Fiber-reinforced composite plates are widely used in aerial vehicles especially as supersonic airfoils in lifting surfaces due to their excellent properties of high stiffness and strength-to-weight ratio. At high aerodynamic pressures, at a certain critical speed, the plate may suffer dynamical instability known as flutter. As in September 1997, when an F-117A fighter lost most of one wing and crashed at an air show due to large amplitude post-flutter responses. Plate flutter is a self-excited oscillation caused by an instability that involves the interaction of aerodynamic, elastic and inertial forces when the aeroelastic damping shifts from a positive to a negative value [1,2].

Since nonlinear aeroelastic problems, especially in the supersonic and hypersonic regimes, play an important role in the safety and flight envelope of aerial vehicles, several analytical and experimental researches have been conducted in this field to explore or enhance the flutter phenomena [3–7]. Most of them, however, focus on a four-edge clamped or simply supported plate undergoing supersonic flow [8]. The analysis methods to carry out the discretization in the spatial domain can generally be categorized into three groups, namely the finite element method (FEM), the Galerkin method and the Rayleigh–Ritz method [9]. Dowell [10] explored the limit cycle oscillations (LCOs) through numerical integration of nonlinear plate flutter equations based on a partial differential equation (PDE)/Galerkin approach. LCOs are a type of aeroelastic instability where the amplitude of oscillations remains bounded and requires time-domain analysis. Reference [11] used the

T. Farsadi (✉) · D. Asadi · H. Kurtaran
Department of Aerospace Engineering, Adana Alparslan Türkeş Science and Technology University, Adana, Turkey
E-mail: tfarsadi@atu.edu.tr

PDE/Rayleigh–Ritz method to explore the chaotic motions of a cantilever plate. Finite element analysis of nonlinear flutter of composite plates was studied by Dixon [12]. Kouchakzadeh et al. [13] applied the classical plate theory along with the von Karman nonlinear strains in structural modeling to analyze the nonlinear aeroelasticity of laminated composite plates in supersonic air flow.

Recently, there has been growing interest in applying curvilinear fibers in composites in order to enhance mechanical properties of structures and to improve flutter boundary instabilities. Initially, the curved fibers were used by Gurdal et al. [14] to vary stiffnesses of rectangular composite plates. Later, Gurdal et al. [15] studied the effects of fiber path definitions on in-plane and out-of-plane response characteristics of flat rectangular variable stiffness laminates. The concept of variable stiffness composites with curvilinear fibers was investigated in several researches [16–20], as in [16–18] optimization of curvilinear fibers was investigated in designing the composite thin-walled beam with bi-convex cross section and [19,20] in composite plates. Kuo [21] investigated the effect of variable stiffness via variable fiber spacing on the supersonic linear flutter of rectangular composite plates using the finite element method (FEM) and quasi-steady aerodynamic Piston theory. Khalafi et al. [22] analyzed free vibration and the linear flutter characteristics of laminated plates under the effects of different changing parameters including boundary condition, skewness, flow direction and layup. Less static deflection, higher buckling loads, failure resistance and natural frequencies, as well as highly enriched nonlinear dynamics, are all the main benefits mentioned in the literature as the advantages of variable stiffness composite laminates (VSCLs) [23]. More recently, Akhavan and Ribeiro [24] investigated nonlinear flutter problem of variable stiffness composite laminates (VSCLs) using p-version finite element method. They considered three boundary conditions types (cantilevered, clamped and simply supported) for one curvilinear fiber configuration.

The present paper examines the nonlinear plate flutter and LCO characteristics of composite plates with curvilinear fiber paths in supersonic flow. Three different types of curvilinear fiber path configurations are introduced here with the goal of improving the flutter and post-flutter behavior of the composite plate. The LCO amplitude diagrams are plotted for the three configurations and compared for non-dimensional critical dynamic pressure and LCO branch behaviors. This research extends the previous study of Akhavan and Ribeiro [23] on aeroelastic analysis of composite plates for a wing-like plate cantilevered at its root. Critical flutter speed is examined according to the variable stiffness concept and then post-flutter phenomena like LCOs and bifurcations diagrams are observed by sweeping the control parameter. From the literature survey on aeroelasticiy of composite plates, few researches have explored the effect of fiber path on the flutter behavior of composite plates [23], and according to the best of the authors' knowledge, this is the second research beside Ref. [24] where the post-flutter behavior of composite plates with variable stiffness concept subject to supersonic aerodynamic is investigated considering curvilinear fibers in the composite structural model. Additionally, in this paper, the aeroelastic critical flutter dynamic pressure of the wing-like plate is improved by exploiting the ideal composite fiber paths using *three* different layup configurations.

In this paper, the governing equation of motion of the composite plate is obtained utilizing the virtual work principle along with the linear first-order aerodynamic piston theory which is used to simulate the loading effects of the supersonic airflow on the plate. According to our previous works [25,26], spatial derivatives in the equation of motion are expressed with the generalized differential quadrature (GDQ) method. Implementing elasticity theory equations, geometric nonlinearity is considered through Von-Karman nonlinear strain–displacement relations. The transverse shear effect is also considered in the equation by application of first-order shear deformation theory. The aeroelastic response of the composite plate is obtained by means of the generalized differential quadrature (GDQ) method. Time integration of the equation of motion is carried out using the Newmark average acceleration method.

In the following, the structural model, underlying equations and simulation results are presented followed by a brief concluding discussion.

2 Theoretical formulations

This section briefly reviews the derivation of the structural model equations, the aerodynamic model, and the methodology for the introduced equations of motions.

2.1 Constitutive equations

The composite wing-like plate structural model presented in this study is similar to that developed in our previous research [25,26]. According to Fig. 1, an orthogonal fixed coordinate system (x, y, z) is placed at the root of a thin plate with a length of b, width of a and thickness of h.
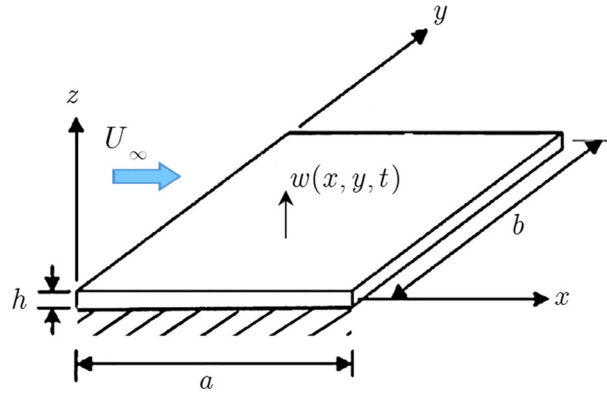
Fig. 1 Plate geometry and coordinate system

The linear displacements of any general point (x, y, z) at time t on the composite plate (u, v, w) are

$$
\begin{aligned}
u(x, y, z, t) &= u_0(x, y, t) + z\theta_x(x, y, t), \\
v(x, y, z, t) &= v_0(x, y, t) + z\theta_y(x, y, t), \\
w(x, y, z, t) &= w_0(x, y, t),
\end{aligned}
\tag{1}
$$

where u_0, v_0 and w_0 are the translations of mid-plane in the x, y and z direction, respectively, and θ_x, θ_y are the rotations about the x, y axes. In this study, geometric nonlinearity is included through von Karman strain–displacement relations [25]:

$$
\varepsilon = \left\{ \begin{array}{c} \varepsilon_x \\ \varepsilon_y \\ \gamma_{xy} \\ \gamma_{yz} \\ \gamma_{zx} \end{array} \right\} = \left\{ \begin{array}{c} \frac{\partial u_0}{\partial x} + \frac{1}{2}\left(\frac{\partial w_0}{\partial x}\right)^2 \\ \frac{\partial v_0}{\partial y} + \frac{1}{2}\left(\frac{\partial w_0}{\partial y}\right)^2 \\ \frac{\partial u_0}{\partial y} + \frac{\partial v_0}{\partial x} + \frac{\partial w_0}{\partial x}\frac{\partial w_0}{\partial y} \\ \theta_y + \frac{\partial w_0}{\partial y} \\ \theta_x + \frac{\partial w_0}{\partial x} \end{array} \right\} + z \left\{ \begin{array}{c} \frac{\partial \theta_x}{\partial x} \\ \frac{\partial \theta_y}{\partial y} \\ \frac{\partial \theta_x}{\partial y} + \frac{\partial \theta_y}{\partial x} \\ 0 \\ 0 \end{array} \right\}.
\tag{2}
$$

In the present study, it is assumed that the strains are moderately large; therefore, only the von Karman nonlinear terms are retained in the strain–displacement relations. In order to investigate very large strain deformations, the whole nonlinear terms should be considered in strain formulations for accuracy in the results [27,28]. In-plane force and moment resultants for a laminated plate can be written as

$$
\left\{ \begin{array}{c} N_x \\ N_y \\ N_{xy} \\ M_x \\ M_y \\ M_{xy} \end{array} \right\} = \left[\begin{array}{cccccc} A_{11} & A_{12} & A_{16} & B_{11} & B_{12} & B_{16} \\ A_{12} & A_{22} & A_{26} & B_{12} & B_{22} & B_{26} \\ A_{16} & A_{26} & A_{66} & B_{16} & B_{26} & B_{66} \\ B_{11} & B_{12} & B_{16} & D_{11} & D_{12} & D_{16} \\ B_{12} & B_{22} & B_{26} & D_{12} & D_{22} & D_{26} \\ B_{16} & B_{26} & B_{66} & D_{16} & D_{26} & D_{66} \end{array} \right] \left\{ \begin{array}{c} \frac{\partial u_0}{\partial x} + \frac{w_0}{R_x} + \frac{1}{2}\left(\frac{\partial w_0}{\partial x}\right)^2 \\ \frac{\partial v_0}{\partial y} + \frac{w_0}{R_y} + \frac{1}{2}\left(\frac{\partial w_0}{\partial y}\right)^2 \\ \frac{\partial u_0}{\partial y} + \frac{\partial v_0}{\partial x} + \frac{\partial w_0}{\partial x}\frac{\partial w_0}{\partial y} \\ \frac{\partial \theta_x}{\partial x} \\ \frac{\partial \theta_y}{\partial y} \\ \frac{\partial \theta_x}{\partial y} + \frac{\partial \theta_y}{\partial x} \end{array} \right\}.
\tag{3}
$$

The equations for transverse shear in terms of the shear force resultant can be stated as

$$
\left\{ \begin{array}{c} Q_y \\ Q_x \end{array} \right\} = \left[\begin{array}{cc} A_{44} & A_{45} \\ A_{45} & A_{55} \end{array} \right] \left\{ \begin{array}{c} \gamma_{yz} \\ \gamma_{zx} \end{array} \right\},
\tag{4}
$$

where A_{ij}, B_{ij}, D_{ij} are stiffness coefficients of the laminate for in-plane, bending stretching coupling, bending and transverse shear stiffness and are derived as

$$\left\{ A_{ij}, B_{ij}, D_{ij} \right\} = \sum_{k=1}^{n} \int_{z_{k-1}}^{z_k} \left\{ 1, z, z^2 \right\} \bar{Q}_{ij}^{(k)} \mathrm{d}z, \quad i, j = 1, 2, 6, \tag{5}$$

$$A_{ij} = \sum_{k=1}^{n} k_i k_j \int_{z_{k-1}}^{z_k} \bar{Q}_{ij}^{(k)} \mathrm{d}z, \quad i, j = 4, 5, \tag{6}$$

where $k_i^2 = 5/6$ ($i = 4, 5$) are the shear correction factors and $\bar{Q}_{ij}^{(k)}$ are the kth layer transformed stiffness coefficients. Moment of inertia properties are stated as:

$$\{I_0, I_1, I_2\} = \sum_{k=1}^{n} \int_{z_{k-1}}^{z_k} \left\{ 1, z, z^2 \right\} \rho^{(k)} \mathrm{d}z, \tag{7}$$

where the kth layer density is denoted by $\rho^{(k)}$.

2.2 Virtual work equation

According to the principle of virtual work, the summation of internal and inertial forces equals the virtual work of external forces. In the absence of structural damping, the equation for laminated plate can be written as [25]

$$\sum_{k=1}^{L} \int_{z_{k-1}}^{z_k} \left[\int_{\Omega} \left\{ \sigma_x^{(k)} \delta\varepsilon_x + \sigma_y^{(k)} \delta\varepsilon_y + \tau_{xy}^{(k)} \delta\gamma_{xy} + \tau_{yz}^{(k)} \delta\gamma_{yz} + \tau_{zx}^{(k)} \delta\gamma_{zx} \right. \right.$$

$$\left. \left. + \rho^{(k)} \left[\left(\ddot{u}_0 + z\ddot{\theta}_x \right) \left(\delta u_0 + z\delta\theta_x \right) + \left(\ddot{v}_0 + z\ddot{\theta}_y \right) \left(\delta v_0 + z\delta\theta_y \right) + \ddot{w}_0 \delta w_0 \right] \right\} \mathrm{d}x\mathrm{d}y \right] \mathrm{d}z$$

$$= \int_{\Omega} p \delta w_0 \mathrm{d}x\mathrm{d}y, \tag{8}$$

where the left-hand side terms in Eq. (8) are inertial forces due to stresses and accelerations, and the right-hand side is the work of aerodynamic loads. Equation (9) is achieved by rewriting the above equation in terms of force and moment resultants as well as mass inertias:

$$\int_{\Omega} [N_x \delta\varepsilon_x^0 + N_y \delta\varepsilon_y^0 + N_{xy} \delta\gamma_{xy}^0 + M_x \delta\varepsilon_x^0 + M_y \delta\varepsilon_y^0 + M_{xy} \delta\gamma_{xy}^0 + Q_y \delta\gamma_{yz}^0$$

$$+ Q_x \delta\gamma_{zx}^0 + (I_0\ddot{u}_0 + I_1\ddot{\theta}_x)\delta u_0 + (I_0\ddot{v}_0 + I_1\ddot{\theta}_y)\delta v_0 + I_1\ddot{w}_0\delta w_0 + (I_1\ddot{u}_0 + I_2\ddot{\theta}_x)\delta\theta_x$$

$$+ (I_1\ddot{v}_0 + I_2\ddot{\theta}_y)\delta\theta_y]\mathrm{d}x\mathrm{d}y = \int_{\Omega} p \delta w_0 \mathrm{d}x\mathrm{d}y. \tag{9}$$

A geometric mapping based on our previous research [25,26] is applied for numerical integral calculations. By implementing the proposed mapping, the Cartesian domain is transformed into a bi-unit square domain. The readers are referred to Ref. [25,26] for the detailed information on the mapping equations.

The effect of structural damping on plates with large deformations was comprehensively investigated previously by Alijani and Amibili [29,30]. Although it is clearly known that instability boundaries can be effectively improved by considering structural damping, this paper investigates the flutter and post-flutter characteristics by considering only the damping due to aerodynamic nature.

2.3 Quasi-steady aerodynamic model

To study the flutter response of the composite plate, the quasi-steady first-order piston aerodynamic method is applied. This method is based on the local motion of the plate that acts as a piston. The air which passes over the plate is presumed to be ideal and isentropic and also has constant specific heat. As assumptions, the local plate motion velocity is much smaller than the airflow velocity and the airflow is parallel to the surface. The first-order piston theory is considered to be [31]

$$P_a = -\frac{2q}{\beta}\left(\frac{\partial w}{\partial x} + \frac{M^2 - 2}{M^2 - 1}\frac{1}{U_\infty}\frac{\partial w}{\partial t}\right), \tag{10}$$

where P_a is the aerodynamic pressure, U_∞ is the free stream velocity, M is the Mach number, q is the dynamic pressure and $\beta = \sqrt{M^2 - 1}$.

The non-dimensional form of the first-order piston method can be introduced as

$$P_a = -\left(\frac{\lambda D_{11}^0}{a^3}\frac{\partial w}{\partial x} + \frac{g_a D_{11}^0}{w_0 a^4}\frac{\partial w}{\partial t}\right), \tag{11}$$

where D_{11}^0 is the bending stiffness matrix when all the fibers of plate are aligned in x-direction, a is the plate width, λ is the non-dimensional dynamic pressure, g_a is the non-dimensional aerodynamic damping, C_a is aerodynamic damping coefficient and w_0 is a reference frequency for a composite plate. The definitions of the mentioned parameters are

$$\lambda = \frac{2qa^3}{\beta D_{11}^0},$$

$$D_{11}^0 = \frac{h^3 E_1^2}{12\left(E_1 - E_2 v_{12}^2\right)},$$

$$g_a = \sqrt{\lambda C_a},$$

$$w_0 = \sqrt{\frac{D_{11}^0}{\rho h a^4}}. \tag{12}$$

2.4 Generalized differential quadrature method

In order to calculate the derivatives of the field variable of Eq. (9), an improved version of the GDQ method is implemented. Before GDQ application, similar to finite difference methods, the laminated plate is discretized to grid points to indicate the points where the field variable values and derivatives are to be calculated. According to the GDQ method, the rth-order derivative of a function $f(\xi)$ with n discrete grid points can be given as

$$\left(\frac{\partial f^r(x)}{\partial \xi^r}\right)_{\xi_i} = \sum_{j=1}^{n} C_{ij}^{(r)} f_j, \tag{13}$$

where ξ_i are discrete points in the variable domain and $C_{ij}^{(r)}$, f_j are weighting coefficients and function values at these points, respectively. The explicit formula for the weight coefficients based on Lagrange polynomial for first-order derivative, i.e., $r = 1$, is

$$C_{ij}^{(1)} = \frac{\Phi(\xi_i)}{(\xi_i - \xi_j)\Phi(\xi_j)} \quad (i \neq j), \tag{14}$$

where

$$\Phi(\xi_i) = \prod_{j=1}^{n} (\xi_i - \xi_j) \quad (i \neq j). \tag{15}$$
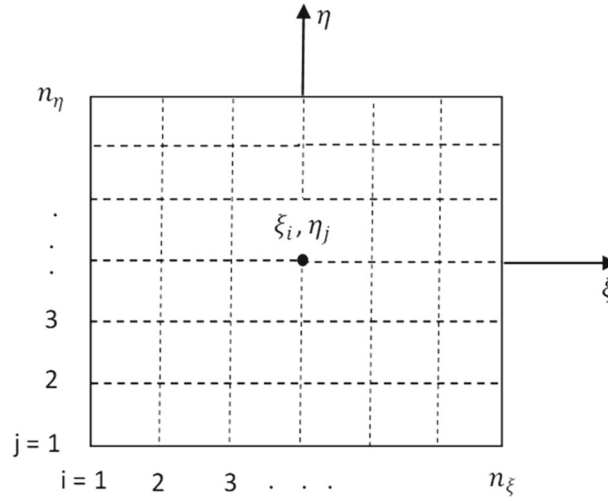
Fig. 2 Grid geometry

The following recursive relations are applied for higher-order derivatives:

$$C_{ij}^{(r)} = r \left[C_{ii}^{(r-1)} C_{ij}^{(1)} - \frac{C_{ij}^{(r-1)}}{(\xi_i - \xi_j)} \right] \quad (i \neq j), \tag{16}$$

$$C_{ii}^{(r)} = - \sum_{\substack{j=1 \\ i \neq j}}^{n} C_{ij}^{(r)}. \tag{17}$$

According to Fig. 2, partial derivatives at a point (ξ_i, η_j) can be defined as follows, where n_ξ and n_η denote grid numbers in ξ and η direction, respectively:

$$\left(\frac{\partial f^r(\xi, \eta)}{\partial \xi^r} \right)_{\xi_i, \eta_j} = \sum_{k=1}^{n_x} C_{kj}^{(r)} f_{kj}, \tag{18}$$

$$\left(\frac{\partial f^s(\xi, \eta)}{\partial \eta^s} \right)_{\xi_i, \eta_j} = \sum_{m=1}^{n_y} C_{im}^{(s)} f_{im}, \tag{19}$$

$$\left(\frac{\partial f^{(r+s)}(\xi, \eta)}{\partial \xi^r \partial \eta^s} \right)_{\xi_i, y_j} = \frac{\partial^r}{\partial \xi^r} \left(\frac{\partial^s f}{\partial \eta^s} \right) = \sum_{k=1}^{n_x} C_{kj}^{(r)} \sum_{m=1}^{n_y} C_{im}^{(s)} f_{km}, \tag{20}$$

where r and s denote derivative orders with respect to the variables ξ and η, respectively.

In Eqs. (21–22), the partial derivatives $\partial f / \partial \xi$ and $\partial f / \partial \eta$ are calculated applying DQM at a grid point:

$$\left(\frac{\partial f}{\partial x} \right)_{ij} = \frac{1}{J_{ij}} \left[\left(\frac{\partial y}{\partial \eta} \right)_{ij} \left(\sum_{k=1}^{n_x} C_{kj}^{(1)} f_{kj} \right) - \left(\frac{\partial y}{\partial \xi} \right)_{ij} \left(\sum_{m=1}^{n_y} C_{im}^{(1)} f_{im} \right) \right], \tag{21}$$

$$\left(\frac{\partial f}{\partial y} \right)_{ij} = \frac{1}{J_{ij}} \left[\left(\frac{\partial x}{\partial \xi} \right)_{ij} \left(\sum_{m=1}^{n_y} C_{im}^{(1)} f_{im} \right) - \left(\frac{\partial x}{\partial \eta} \right)_{ij} \left(\sum_{k=1}^{n_x} C_{kj}^{(1)} f_{kj} \right) \right]. \tag{22}$$

2.5 Solution method

Plate domain discretization with grid points, applying the GDQ method for calculating partial derivatives at grid points, and using the Gauss–Lobatto quadrature rule to evaluate the integrals in the virtual work, result in the matrix form of the equation of motion as

$$\mathbf{M\ddot{U} + P = F,} \tag{23}$$

where $\mathbf{M}$ indicates the mass matrix and $\mathbf{F}$, $\mathbf{P}$ and $\mathbf{\ddot{U}}$ define external force, internal force and acceleration vectors, respectively. The plate's transient response is evaluated by applying the time integration scheme of implicit Newmark constant average acceleration.

According to the Newmark approach, at the $(n + 1)$th time step, i.e., at time $(n + 1)\Delta t$ or $tn + 1$, the equation of motion is stated as

$$\mathbf{M\ddot{U}}_{n+1} + \mathbf{P}_{n+1} = \mathbf{F}_{n+1}. \tag{24}$$

Then, replacing the velocity and acceleration terms as

$$\mathbf{\ddot{U}}_{n+1} = C_0 (\mathbf{U}_{n+1} - \mathbf{U}_n) - C_1\mathbf{\dot{U}}_n - \mathbf{\ddot{U}}_n, \tag{25}$$

$$\mathbf{\dot{U}}_{n+1} = \mathbf{\dot{U}}_n + \Delta t\mathbf{\ddot{U}}_n + \frac{\Delta t}{2}\left(\mathbf{\dot{U}}_{n+1} - \mathbf{\ddot{U}}_n\right), \tag{26}$$

where $C_0 = 4/\Delta t^2$, $C_1 = 4/\Delta t$ and $\mathbf{U}_n$ denotes the displacements at the nth time step, Eq. (24) can be rewritten as:

$$C_0\mathbf{M U}_{n+1} + \mathbf{P}_{n+1} = \mathbf{F}_{n+1} + \mathbf{M}(C_0\mathbf{U}_n + C_1\mathbf{\dot{U}}_n + \mathbf{\ddot{U}}_n). \tag{27}$$

All the right-hand side expressions of Eq. (27) are known from the solution of this equation at the nth time step. Since Eq. (27) is nonlinear in terms of unknown displacements $Un + 1$, an iterative method like Newton–Raphson is applied for the solution. To achieve the solution of Eq. (27), it is expressed in terms of residual forces or error function $R_n + 1$ as:

$$\mathbf{R}_{n+1} = \mathbf{F}_{n+1} + \mathbf{M}\left(C_0\mathbf{U}_n + C_1\mathbf{\dot{U}}_n + \mathbf{\ddot{U}}_n\right) - C_0\mathbf{M U}_{n+1} - \mathbf{P}_{n+1}. \tag{28}$$

If $\mathbf{U}_{n+1}^i$ is an approximate trial solution at the ith iteration leading to error $\mathbf{R}_{n+1}^i$, an improved solution $\mathbf{U}_{n+1}^{i+1}$ can be obtained using linear Taylor series expansion of $\mathbf{R}_{n+1}^{i+1}$ and equating it to zero as below:

$$\mathbf{R}_{n+1}^{i+1} \approx \mathbf{R}_{n+1}^i + \mathbf{K}_{n+1}^i(\mathbf{U}_{n+1}^{i+1} - \mathbf{U}_{n+1}^i) = 0, \tag{29}$$

where $\mathbf{K}_{n+1}^i$ is referred to as tangent stiffness matrix. Equation (29) can be written in incremental form as

$$\mathbf{K}_{n+1}^i\Delta\mathbf{U}_{n+1}^i = -\mathbf{R}_{n+1}^i, \tag{30}$$

where $\Delta\mathbf{U}_{n+1}^i$ is the displacement increment in the current iteration given as:

$$\Delta\mathbf{U}_{n+1}^i = \mathbf{U}_{n+1}^{i+1} - \mathbf{U}_{n+1}^i. \tag{31}$$

The improved solution at $(i + 1)$th iteration is defined as:

$$\mathbf{U}_{n+1}^{i+1} = \mathbf{U}_{n+1}^i + \Delta\mathbf{U}_{n+1}^i. \tag{32}$$

The iterative solution procedure is repeated until the error function $\mathbf{R}_{n+1}^{i+1}$ is sufficiently close to zero. To start the Newton Raphson solution procedure, initial acceleration values $\mathbf{\ddot{U}_0}$ are computed by using initial displacements $\mathbf{U_0}$ and velocities $\mathbf{\dot{U}_0}$ at time zero ($t = 0$).

3 Description of variable stiffness

Advances in manufacturing techniques such as the tow placement machines make it possible to spatially vary the fiber orientation within a single lamina. Figure 3a–c illustrates three different variable stiffness composite laminates (VSCLs) defined by curvilinear fiber path functions of $\theta_1, \theta_2, \theta_3$. The curvilinear fiber path function determines the ply angle measured from the positive x-axis at a point of the plate. In order to better categorize the name of the configurations, here and after, variable stiffness composite laminates with fiber paths $\theta_1, \theta_2, \theta_3$ are labeled as VSCL_1, VSCL_2 and VSCL_3, respectively. The formulations of the fiber path variation for each layup configuration are presented in Eqs. (33–35). The fibers start from a reference point with a fiber orientation angle T_0 and change along the x axis and y axis, until the fiber orientation angle reaches a value T_1 at a characteristic distance a and b from the reference point as the path definitions are formulated in Eqs. (33–35). According to Fig. 3a–c and the related equations given in (33–35), θ_1 is changing along the x axis, θ_2 changes
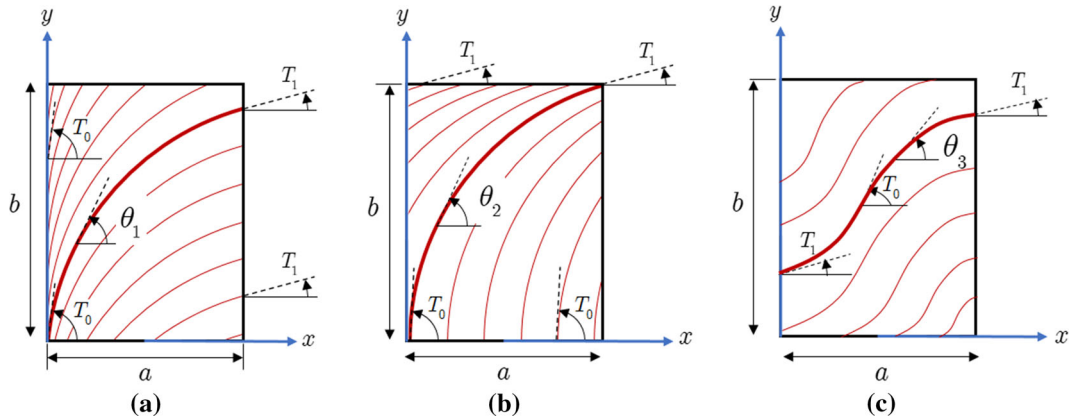
Fig. 3 Curvilinear fiber paths. **a** VSCL_1, **b** VSCL_2, **c** VSCL_3

Table 1 Comparison of natural frequencies of VSCL with curvilinear fibers

VSCL plate	Method	Mode		
		1	2	3
$[\langle 0, 45 \rangle , \langle -45, 60 \rangle , \langle 0, 45 \rangle]$				
Simply supported	Ref. [19]	358.488	589.9	960.361
	Present study	351.622	581.41	954.14
Clamped	Ref. [19]	579.398	821.532	1225.79
	Present study	579.745	822.601	1227.56
$[\langle 30, 0 \rangle , \langle 45, 90 \rangle , \langle 30, 0 \rangle]$				
Simply supported	Ref. [19]	308.799	503.799	845.509
	Present study	307.62	504.11	846.79
Clamped	Ref. [19]	667.177	862.919	1234.64
	Present study	665.217	863.689	1238.5
$[\langle 90, 45 \rangle , \langle 60, 30 \rangle , \langle 90, 45 \rangle]$				
Simply supported	Ref. [19]	329.688	539.407	886.392
	Present study	323.99	533.1	880.587
Clamped	Ref. [19]	710.77	912.183	1335.49
	Present study	709.46	915.47	1340.98

Table 2 Geometric and material properties

a (m)	b (m)	h (m)	E_1 (GPa)	E_2 (GPa)	G_{12} (GPa)	G_{13} (GPa)	G_{23} (Gpa)	υ_{12}	ρ (kg/m^3)
1	1	0.01	*173*	7.2	3.76	*3.76*	3.76	0.29	1540

Table 3 Material properties

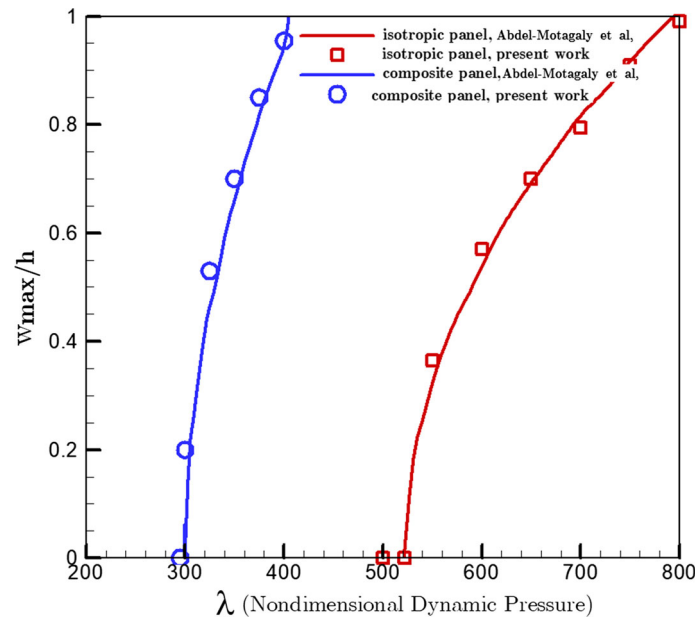| Property	Value
Isotropic (aluminum)	
E	72.4 GPa
υ	0.3
ρ	2700 kg/m^3
Composite (graphite/epoxy)	
E_1	155.1 GPa
E_2	8.1 GPa
G_{12}	4.6 GPa
G_{23}	3.0 GPa
υ_{12}	0.22
ρ	1550 kg/m^3

Fig. 4 Comparison of LCO amplitudes of simply supported square plates

Table 4 Geometric and material properties

a (m)	b (m)	h (m)	E_1 (GPa)	E_2 (GPa)	G_{12} (GPa)	G_{13} (GPa)	G_{23} (GPa)	v_{12}	ρ (kg/m^3)
0.6	0.6	0.006	126.3	8.76	3.76	3.35	3.35	0.334	1557

along the y axis, and θ_3 changes from T_0 to T_1 symmetrically from the midpoint of each ply. Thus, the two design variables T_0 and T_1 in each layer are required to determine the variation of the fiber orientation on the surface of each layup.

For VSCL_1;

$$\theta_1 = T_0 + (T_1 - T_0)\left(\frac{x}{a}\right) \tag{33}$$

For VSCL_2;

$$\theta_2 = T_0 + (T_1 - T_0)\left(\frac{y}{b}\right) \tag{34}$$

And for VSCL_3;

$$\theta_3 = T_0 + 2(T_1 - T_0)\left(\frac{\left|x - \frac{a}{2}\right|}{a}\right) \tag{35}$$

4 Numerical results

In this section, the above formulation is applied and numerical results are presented for the aeroelastic responses of each curvilinear fiber path function (VSCL_1, VSCL_2 and VSCL_3) of the composite plate. In order to verify the variable stiffness structural and aeroelastic model, the natural frequencies of our model is compared with credible references and then the post-flutter behavior and the LCO are examined. To investigate the effect of the fiber path function on the aeroelastic characteristics of the composite plate, the ideal fiber path
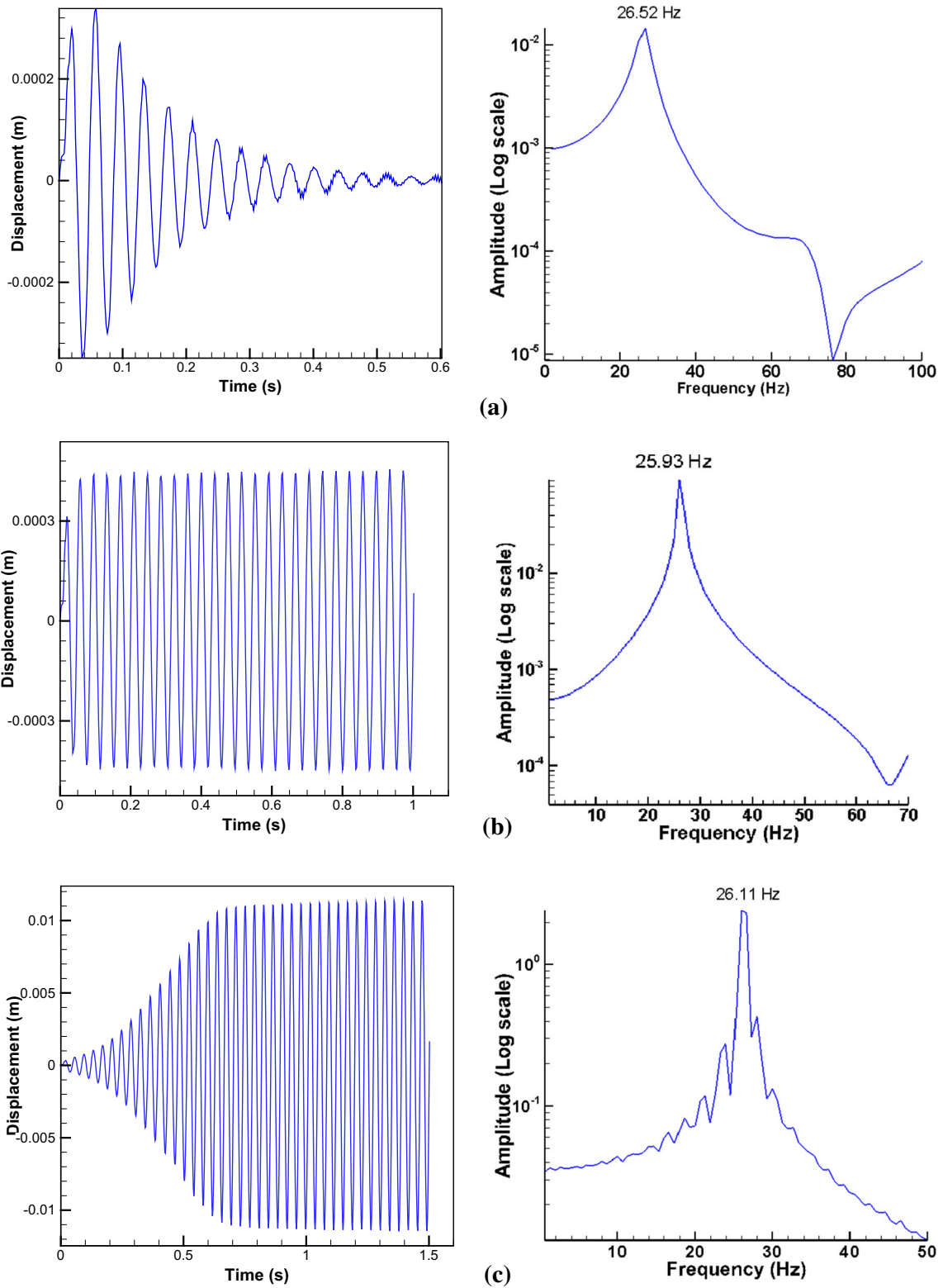
Fig. 5 Time and frequency response qualifications of the vertical tip deflection of VSCL_1 case, fiber design parameters $\langle T_0 = 0, T_1 = 0 \rangle$. **a** Subcritical ($\lambda = 26$), **b** critical ($\lambda_{cr} = 26.875$), **c** supercritical ($\lambda_{cr} = 28$)
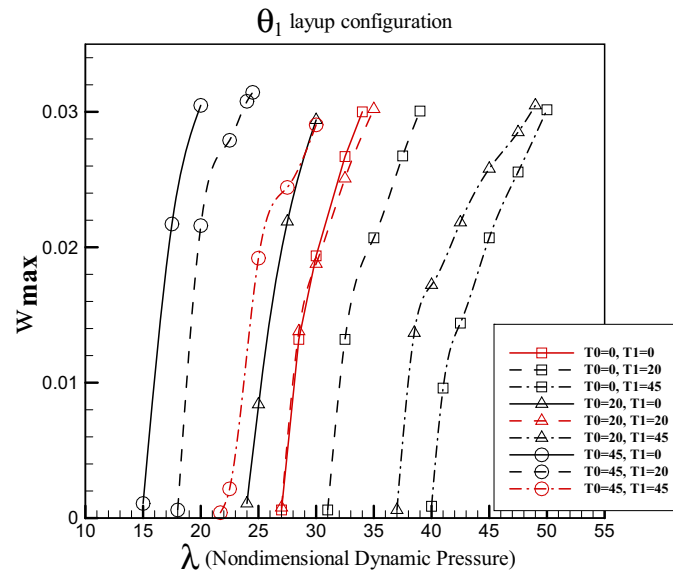
Fig. 6 The effect of fiber path on the LCO amplitude diagram of the VSCL_1 plate (branches in red are unidirectional cases) (color figure online)

Table 5 Critical non-dimensional dynamic pressure for various angle sets of the VSCL_1 plate

	$T_0 = 0$			$T_0 = 20$			$T_0 = 45$		
	$T_1 = 0$	$T_1 = 20$	$T_1 = 45$	$T_1 = 0$	$T_1 = 20$	$T_1 = 45$	$T_1 = 0$	$T_1 = 20$	$T_1 = 45$
λ_{cr}	26.9	30.5	39.85	23.2	26.45	36.35	14.6	17.1	21

is calculated in three different layup configurations named VSCL_1, VSCL_2 and VSCL_3. The goal here is to find the ideal fiber path angle to reach the maximum flutter pressure and good post-flutter limit cycle oscillation (LCO) behavior of the wing-like plate tip.

4.1 Structural model validation

The first three natural frequencies of VSCL plate with curvilinear fiber path are compared with the results of Ref. [19] in Table 1. In Ref. [19], the p-version FEM and third-order shear deformation are employed. Table 1 shows the comparison of frequencies for a three-layer simply supported and clamped VSCL and fiber orientation angles defined by $\langle T_0, T_1 \rangle$. The geometric and material properties are given in Table 2.

In order to verify the present nonlinear aeroelastic model and solution methodology, the results of Abdel-Motagaly et al. [32] are used for comparison in two cases of isotropic and composite plates. The FEM time-domain approach is presented in Ref. [32] for studying the nonlinear plate flutter characteristics. Isotropic and composite material properties are given in Table 3.

The validation includes calculation of the LCO amplitude of plate flutter for simply supported square (0.305, 0.305, 0.0013 m) isotropic plate and (0.305, 0.305, 0.0012 m) composite plate with eight layers $[0/45/-45/90]_S$. The aerodynamic damping coefficient C_a is set to 0.1 for both isotropic and composite plate structures. Figure 4 demonstrates good agreement between the present method and Ref. [32] for LCO amplitudes of both isotropic and composite plates.

4.2 Time-domain analysis

For the variable stiffness composite plate, nonlinear aeroelastic analyses have been performed by the Newmark constant average acceleration time integration scheme. The nonlinear transient response of a square laminated
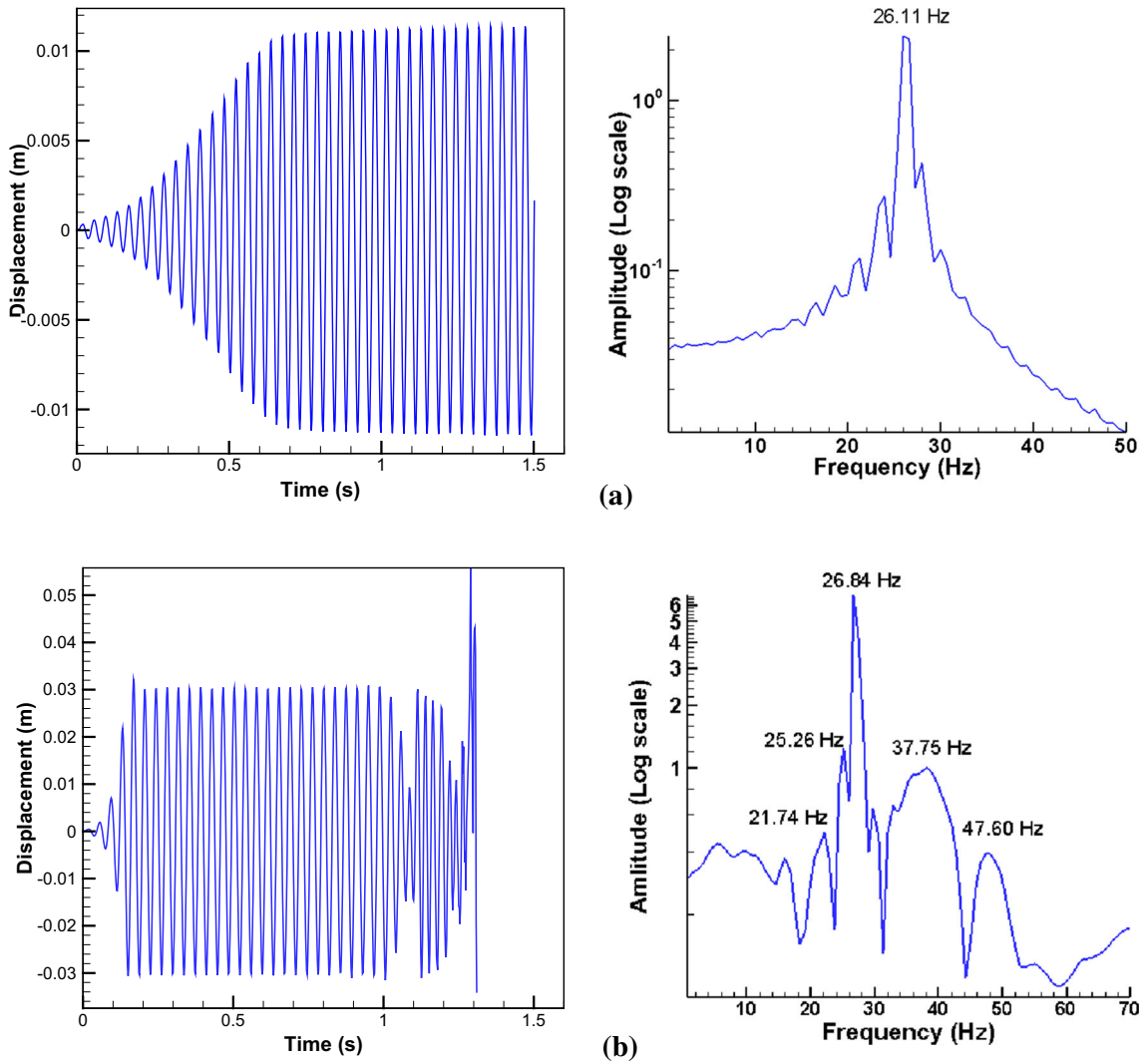
Fig. 7 Time and frequency response qualification of the vertical tip deflection of VSCL_1 case, fiber design parameters $\langle T_0 = 0, T_1 = 0 \rangle$ at **a** $\lambda = 1.002\lambda_{\text{cr}}$ **b** $\lambda = 1.2\lambda_{\text{cr}}$

composite plate with three layup configurations of VSCL_1, VSCL_2 and VSCL_3 is shown in Fig. 3. Cantilevered boundary condition with one side clamped and three side free edges has been considered. Square plate dimensions along with material properties are given in Table 4. The stacking scheme for composite layers is in the form of Ref. [23] given as:

$$[45 + \langle T_0, T_1 \rangle, -45 - \langle T_0, T_1 \rangle, \langle T_0, T_1 \rangle, -\langle T_0, T_1 \rangle, 90 + \langle T_0, T_1 \rangle, -90 - \langle T_0, T_1 \rangle]_{\text{sym}}, \qquad (36)$$

where $\langle T_0, T_1 \rangle$ are reference fiber angles shown in Fig. 3 for curvilinear fiber paths of VSCL_1, VSCL_2 and VSCL_3. The fiber angles $\langle T_0, T_1 \rangle$ can also be considered as design parameters.

For transient analysis, a time step value of $dt = 2$ ms is used. It is assumed that the composite plate is initially at rest and the plate is given an initial disturbance to vertical displacement w. Due to the intrinsic character of aeroelastic systems which fall in the category of self-excited vibrations, imposing a small variation of initial condition may ultimately lead to attenuation or magnification of the response. In cases where the steady-state aeroelastic response damps out, the system is stable. On the contrary, for unstable conditions, limit cycle oscillations appear. In the following, time history plots are given for the maximum tip displacement of the plate at $\eta = 1$, $\xi = 0.75$.

Figure 5a–c illustrates the time history of a nonlinear analysis of vertical plate displacement at the subcritical, critical and supercritical non-dimensional dynamic pressure λ given in Eq. (12) for the case VSCL_1
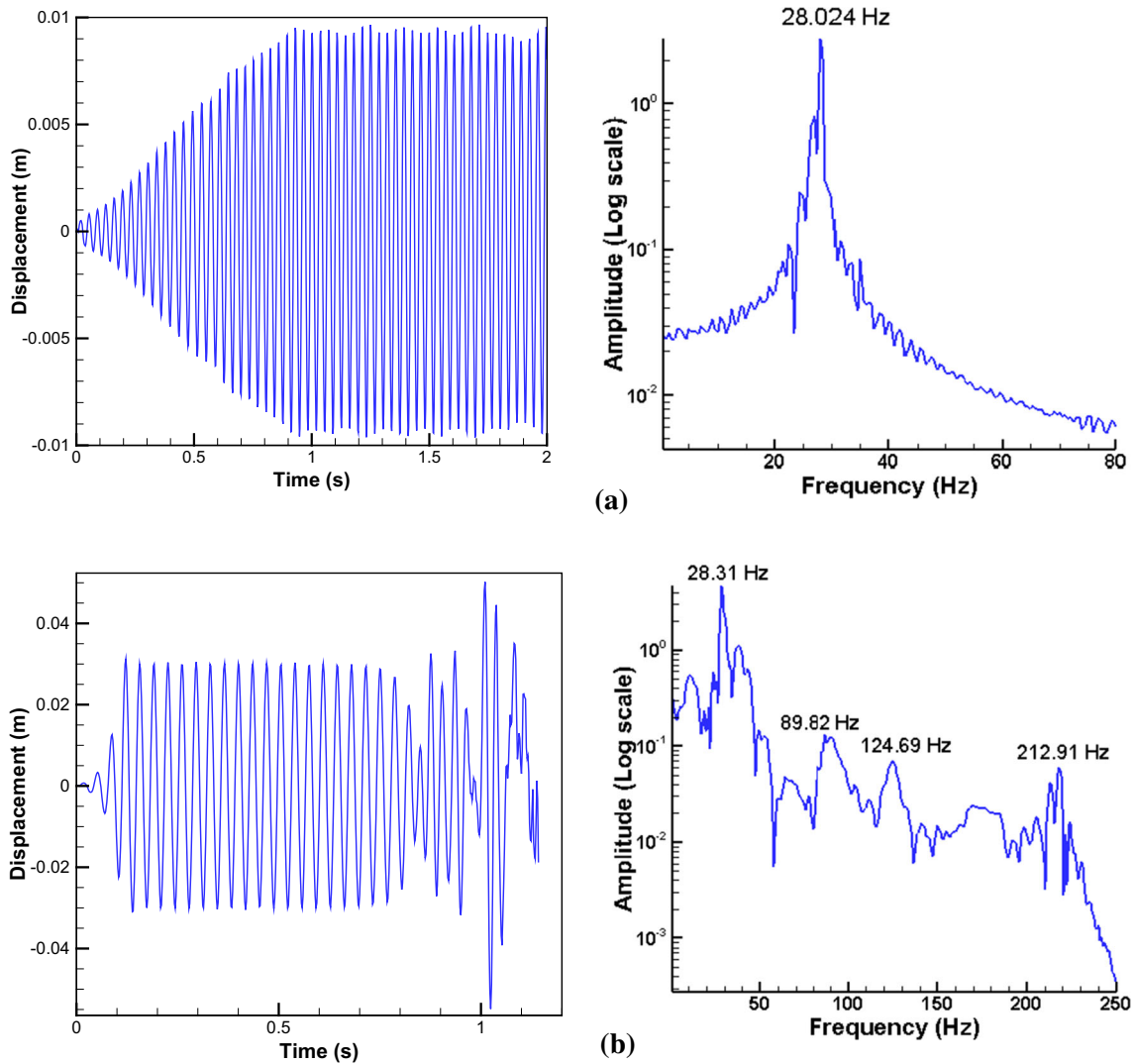
Fig. 8 Time and frequency response qualification of the vertical tip deflection of the VSCL_1 case, fiber design parameters $\langle T_0 = 0, T_1 = 45 \rangle$ at **a** $\lambda = 1.002\lambda_{cr}$ **b** $\lambda = 1.25\lambda_{cr}$

(Fig. 3a and Eq. (33)) with $\langle T_0 = 0, T_1 = 0 \rangle$). As depicted in Fig. 5a, in a nonlinear analysis of subcritical λ value, disturbance generated by the imposed initial conditions is attenuated due to the aerodynamic damping. With the increase in λ, LCO shown in Fig. 5b starts at the bifurcation pressure which corresponds to the critical non-dimensional dynamic pressure λ_{cr}. As illustrated in Fig. 5c, beyond the λ_{cr}, in the supercritical region, amplitude of LCO increases substantially and the magnitude of oscillations of tip vertical deflection is much higher than the magnitude of the oscillations at the critical condition.

4.3 Fiber angle study

LCO amplitude diagrams of composite plate with θ_1 configuration (VSCL_1 case) are presented in Fig. 6 for set of fiber design angles of $\langle T_0 = \{0, 20, 45\}, T_1 = \{0, 20, 45\} \rangle$. Bifurcation points identified by the nonlinear aeroelastic analysis as critical non-dimensional dynamic pressure (λ_{cr}) are given in Table 5. The highest critical non-dimensional pressure is seen for $\langle T_0 = 0, T_1 = 45 \rangle$ which is almost 33% higher than the closest unidirectional fiber path with $\langle T_0 = 0, T_1 = 0 \rangle$ as shown in red with square symbols in Fig. 6.

Figure 6 demonstrates that for the fiber design angle set of $\langle T_0 = 0, T_1 = 45 \rangle$ and $\langle T_0 = 20, T_1 = 45 \rangle$, not only the instability occurs at a higher λ values, but the post-flutter response of the plate tip is also slightly well
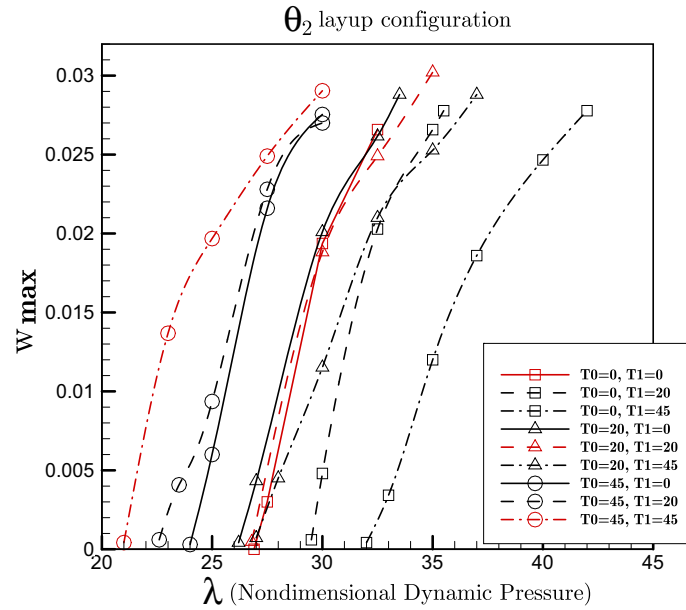
Fig. 9 The effect of fiber path on the LCO amplitude diagram of the VSCL_2 plate (branches in red are unidirectional cases) (color figure online)
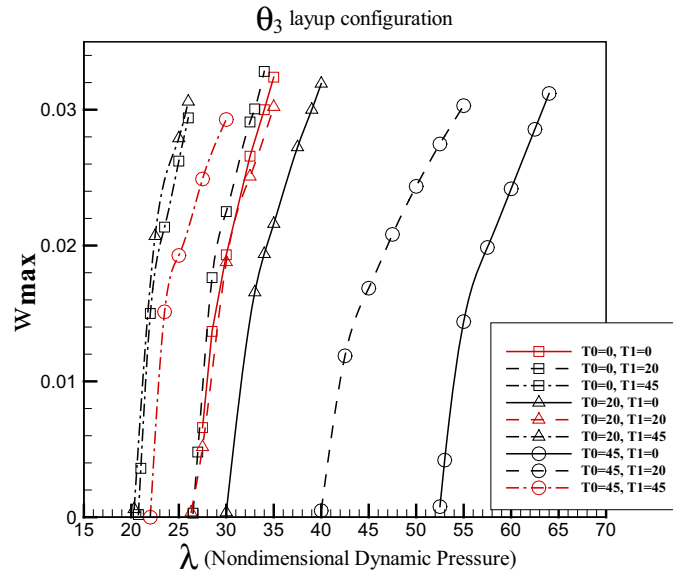

Fig. 10 The effect of fiber path on the LCO amplitude diagram of the VSCL_3 plate (branches in red are unidirectional cases) (color figure online)

behaved compared to the counterpart unidirectional fiber design sets, $\langle T_0 = 0, T_1 = 0 \rangle$ and $\langle T_0 = 20, T_1 = 20 \rangle$ as shown in red with square and triangular symbols, respectively.

In order to compare the time response of the unidirectional and curvilinear fiber paths in the post-flutter range, beginning from low λ values to the highest values, two fiber design sets, $\langle T_0 = 0, T_1 = 0 \rangle$ as unidirectional set and $\langle T_0 = 0, T_1 = 45 \rangle$ as curvilinear fiber set in the case VSCL_1 are studied. It should be noted that at low λ values in the post-flutter range, responses are periodic and for values which are sufficiently higher than the critical λ values, nonlinear aeroelastic responses may become chaotic. For the composite plate VSCL_1 of unidirectional fiber design set $\langle T_0 = 0, T_1 = 0 \rangle$, Figs. 7 and 8 present the time response and frequency plots for vertical displacement of the plate tip, for non-dimensional dynamic pressure ratios of 1.002 and 1.2,

Table 6 Critical non-dimensional dynamic pressure for various angle sets of the VSCL_2 plate

| | $T_0 = 0$ | | | $T_0 = 20$ | | | $T_0 = 45$ | | |
	$T_1 = 0$	$T_1 = 20$	$T_1 = 45$	$T_1 = 0$	$T_1 = 20$	$T_1 = 45$	$T_1 = 0$	$T_1 = 20$	$T_1 = 45$
λ_{cr}	26.9	28.7	31.9	25.85	26.45	26.75	24	22.2	21

Table 7 Critical non-dimensional dynamic pressure for various angle sets of the VSCL_3 plate

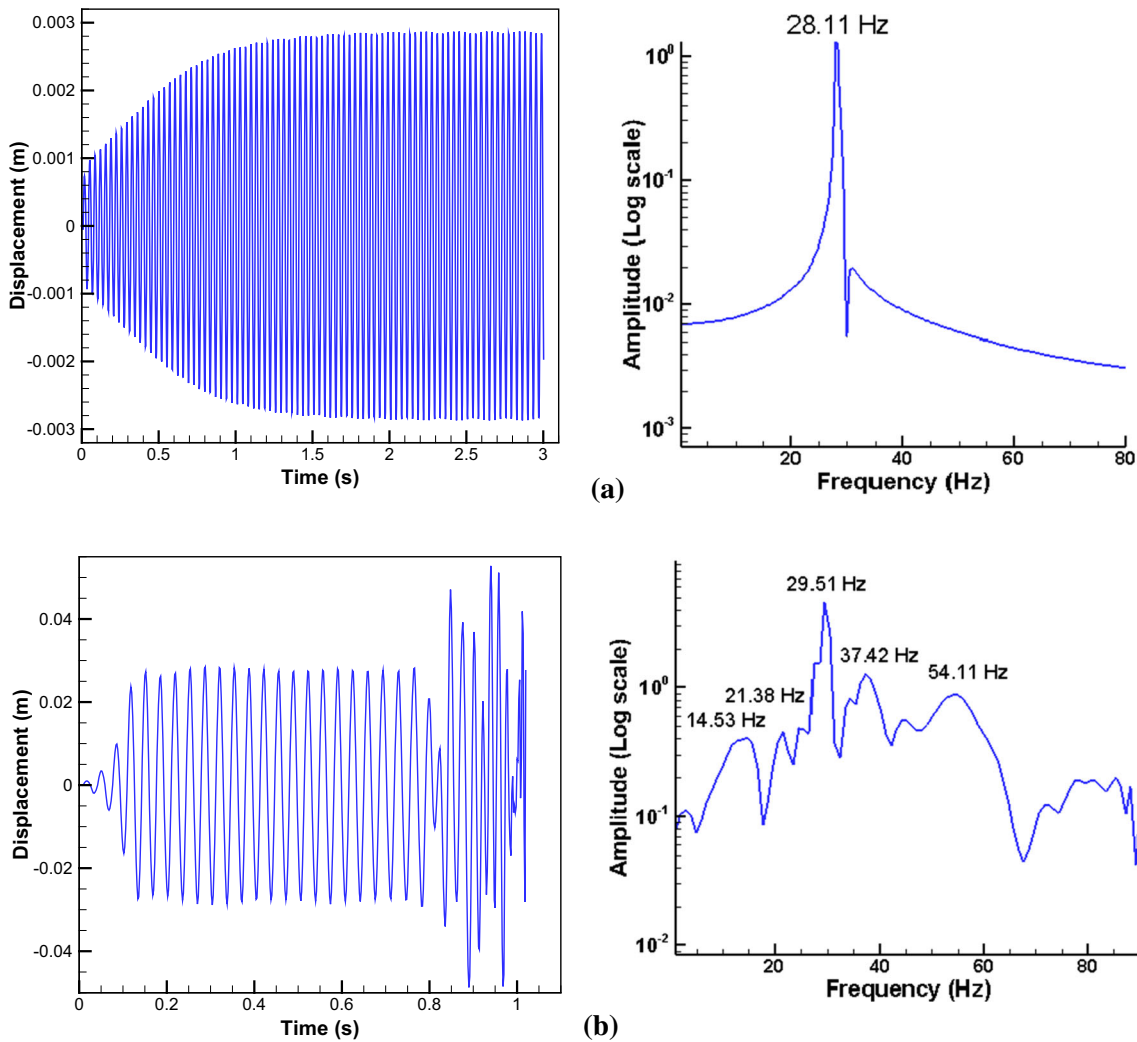| | $T_0 = 0$ | | | $T_0 = 20$ | | | $T_0 = 45$ | | |
	$T_1 = 0$	$T_1 = 20$	$T_1 = 45$	$T_1 = 0$	$T_1 = 20$	$T_1 = 45$	$T_1 = 0$	$T_1 = 20$	$T_1 = 45$
λ_{cr}	26.9	26.8	20.75	30	26.45	20.5	52.1	40	21

Fig. 11 Time and frequency response qualification of the vertical tip deflection of VSCL_3 case, fiber design parameters $\langle T_0 = 45, T_1 = 0 \rangle$ at **a** $\lambda = 1.002\lambda_{cr}$ **b** $\lambda = 1.2\lambda_{cr}$

respectively. Figure 7a shows, at low post-critical pressure ratio of $\lambda = 1.002\lambda_{cr}$, that the nonlinear aeroelastic response of the plate is purely periodic with distinct frequency in the FFT plot. For higher post-flutter pressure ratio of $\lambda = 1.2\lambda_{cr}$, the nonlinear aeroelastic response of the plate is chaotic as seen from the time and frequency responses in Fig. 7b.

Figure 8 depicts the time response and frequency plot for the vertical tip displacements of the VSCL_1 configuration for curvilinear fiber set of $\langle T_0 = 0, T_1 = 45 \rangle$, for values of $\lambda = 1.002\lambda_{cr}$ and $\lambda = 1.25\lambda_{cr}$, which is the final value of the post-flutter range, respectively. Comparing Figs. 7b and 8b clarifies that, chaotic motion occur in higher ratios of pressure ($l = 1.2$ for $\langle T_0 = 0, T_1 = 0 \rangle$ and $l = 1.25$ for $\langle T_0 = 0, T_1 = 45 \rangle$) for the curvilinear plate respecting unidirectional case.

Figures 9 and 10 illustrate the LCO diagrams which demonstrate the effect of the fiber improvement on the flutter and post-flutter characteristics of the VSCL_2 and VSCL_3 plates, respectively. Figure 10 reveals that for the design of unidirectional fiber set of $\langle T_0 = 0, T_1 = 0 \rangle$, the bifurcation angle is wide and the amplitude of the LCO increases abruptly with a slight increase in the dynamic pressure. In this design, the nonlinearity is relatively weak and the amplitude curves are nearly vertical. On the other hand, for the curvilinear fiber sets of $\langle T_0 = 45, T_1 = 0 \rangle$ and $\langle T_0 = 45, T_1 = 20 \rangle$, the bifurcation angle is slightly lower and the amplitude of the LCO is confined within a band as the dynamic pressure increases. Such a supercritical post-flutter behavior, which is a sign of strong nonlinearity, is actually a desirable nonlinear aeroelastic response. Tables 6 and 7 represent the critical dynamic pressure determined by the nonlinear aeroelastic solution.

Comparing flutter dynamic pressures given in Tables 5, 6 and 7 and LCO amplitude diagrams shown in Figs. 6, 9 and 10 for the different plate configurations VSCL_1, VSCL_2 and VSCL_3, one can see that for the curvilinear fiber design set $\langle T_0 = 45, T_1 = 0 \rangle$ of the VSCL_3 configuration, the flutter dynamic pressure is the highest and is 48.4% higher than for the closest unidirectional case. The highest curvilinear fiber set is followed by the fiber sets of $\langle T_0 = 0, T_1 = 45 \rangle$ for VSCL_1 and $\langle T_0 = 45, T_1 = 20 \rangle$ for VSCL_3 as second and third highest critical dynamic pressure with $\lambda_{cr} = 39.85$ and $\lambda_{cr} = 40$, respectively.

For the VSCL_3 configuration with curvilinear fiber set $\langle T_0 = 45, T_1 = 0 \rangle$, which has the highest λ_{cr} among the all fiber sets, Fig. 11 gives the time histories of the vertical displacements of the plate tip and its respective frequency response plot at post-flutter λ values of $\lambda = 1.002\lambda_{cr}$ and $\lambda = 1.2\lambda_{cr}$. From Fig. 11a, it is inferred that for low post-flutter λ values ($\lambda = 1.002\lambda_{cr}$), the aeroelastic response is purely periodic and the frequency response has a distinct frequency value. Finally, according to Fig. 11b, at the post-flutter dynamic pressure ratio of $\lambda = 1.2\lambda_{cr}$, nonlinear aeroelastic response becomes chaotic and the frequency response plot shows that a broadband range of dominant frequencies exists in the response.

It was shown that the curvilinear fiber placement can create a more efficient aeroelastic performance in cantilevered rectangular plates; therefore, it can be considered in aeroelastic studies of composite panels with different geometries and boundary conditions [33–35].

5 Conclusion

An advanced curvilinear fiber layup is utilized to enhance the aeroelastic performance of wing-like plates. For this aim, a design tool is developed using the composite plate theory which considers the nonlinear strains for the structural modeling of the cantilevered plate and the first-order piston theory for the supersonic quasi-steady aerodynamic modeling of the plate. Three curvilinear fiber layup configurations (VSCL_1, VSCL_2 and VSCL_3) are considered to choose the best configuration of the fiber for maximum instability dynamic pressure and post-flutter performance. The GDQ method was applied to obtain the nonlinear aeroelastic transient response of laminated composite plates. It was shown that the different curvilinear fiber configurations and ply angle with different design parameters have a major influence on the nonlinear aeroelastic characteristics including the LCO and bifurcation diagrams. This can be explained by aeroelastic concepts such as wash-in/wash-out and linear and nonlinear stiffness characteristics. Numerical results demonstrate the advantages of variable stiffness composite laminates (VSCL) over the unidirectional fiber model in terms of instability and LCO behavior. Additionally, the best VSCL configuration was introduced for improved post-flutter responses.

References

1. Dowell, E.H.: Nonlinear Aeroelasticity: A Modern Course in Aeroelasticity, Solid Mechanics and Its Applications, vol. 217. Springer, Cham (2015)
2. Farsadi, T., Rahmanian, M., Kayran, A.: Geometrically nonlinear aeroelastic behavior of pretwisted composite wings modeled as thin walled beams. J. Fluids Struct. **83**, 259–292 (2018)
3. Tian, W., Yang, Z., Gu, Y., Wang, X.: Analysis of nonlinear aeroelastic characteristics of a trapezoidal wing in hypersonic flow. Nonlinear Dyn. **89**(2), 1205–1232 (2017)
4. Katsikadelis, J.T., Babouskos, N.G.: Flutter instability of laminated thick anisotropic plates using BEM. Acta Mech. **229**(2), 613–628 (2018)

5. Zhao, M.H., Zhang, W.: Nonlinear dynamics of composite laminated cantilever rectangular plate subject to third-order piston aerodynamics. Acta Mech. **225**(7), 1985–2004 (2014)
6. Abbas, L.K., Rui, X., Marzocca, P., et al.: A parametric study on supersonic/hypersonic flutter behavior of aero-thermo-elastic geometrically imperfect curved skin panel. Acta Mech. **222**, 41–57 (2011)
7. Li, F.M., Song, Z.G.: Aeroelastic flutter analysis for 2D Kirchhoff and Mindlin panels with different boundary conditions in supersonic airflow. Acta Mech. **225**(12), 3339–3351 (2014)
8. Xie, D., Xu, M., Dai, H., Dowell, E.H.: Observation and evolution of chaos for a cantilever plate in supersonic flow. J. Fluids Struct. **50**(2), 271–291 (2014)
9. Xie, D., Xu, M., Dai, H., Dowell, E.H.: Proper orthogonal decomposition method for analysis of nonlinear panel flutter with thermal effects in supersonic flow. J. Sound Vib. **337**, 263–283 (2015)
10. Dowell, E.H.: Nonlinear oscillations of a fluttering plate. AIAA J. **4**, 1267–1275 (1966)
11. Xie, D., Xu, M., Dai, H., Dowell, E.H.: Observation and evolution of chaos for a cantilever plate in supersonic flow. J. Fluids Struct. **50**, 271–291 (2014)
12. Dixon, I., Mei, C.: Finite element analysis of large amplitude panel flutter of thin laminates. AIAA J. **4**(31), 701 (1993)
13. Kouchakzadeh, M.A., Rasekh, M., Haddadpour, H.: Panel flutter analysis of general laminated composite plates. Compos. Struct. **92**, 2906–2915 (2010)
14. Gurdal, Z., Olmedo, R.: In-plane response of laminates with spatially varying fiber orientations: variable stiffness concept. AIAA J. **31**(4), 751–758 (1993)
15. Gürdal, Z., Tatting, B.F., Wu, C.K.: Variable stiffness composite panels: effects of stiffness variation on the in-plane and buckling response. Compos. Part A Appl. Sci. Manuf. **39**, 911–922 (2008)
16. Zamani, Z., Haddadpour, H., Ghazavi, M.: Curvilinear fiber optimization tools for design thin walled beams. Thin-Walled Struct. **49**(3), 448–454 (2011)
17. Haddadpour, H., Zamani, Z.: Curvilinear fiber optimization tools for aeroelastic design of composite wings. J. Fluids Struct. **33**, 180–190 (2012)
18. Gunay, M.G., Timarci, T.: Static analysis of thin-walled laminated composite closed-section beams with variable stiffness. Compos. Struct. **182**, 67–78 (2017)
19. Akhavan, H., Ribeiro, P.: Natural modes of vibration of variable stiffness composite laminates with curvilinear fibers. Compos. Struct. **93**(11), 3040–3047 (2011)
20. Fazilati, J.: Panel flutter of curvilinear composite laminated plates in the presence of delamination. J. Compos. Mater. **52**(20), 2789–2801 (2018)
21. Kuo, S.Y.: Flutter of thermally buckled angle-ply laminates with variable fiber spacing. J. Compos. Part B **95**, 240–251 (2016)
22. Khalafi, V., Fazilati, J.: Supersonic panel flutter of variable stiffness composite laminated skew panels subjected to yawed flow by using NURBS-based isogeometric approach. J. Fluids Struct. **82**, 198–214 (2018)
23. Akhavan, H., Ribeiro, P.: Aeroelasticity of composite plates with curvilinear fibers in supersonic flow. Compos. Struct. **194**, 335–344 (2018)
24. Akhavan, H., Ribeiro, P.: Reduced-order models for nonlinear flutter of composite laminates with curvilinear fibers. AIAA J. **57**(7), 1–14 (2019)
25. Kurtaran, H.: Large displacement static and transient analysis of functionally graded deep curved beams with generalized differential quadrature method. Compos. Struct. **131**, 821–831 (2015)
26. Kurtaran, H.: Geometrically nonlinear transient analysis of thick deep composite curved beams with generalized differential quadrature method. Compos. Struct. **128**, 241–250 (2015)
27. Amibili, M.: Nonlinear Mechanics of Shells and Plates: Composite, Soft and Biological Materials. Cambridge University Press, New York (2018)
28. Alijani, F., Amabili, M.: Non-linear static bending and forced vibrations of rectangular plates retaining non-linearities in rotations and thickness deformation. Int. J. Non-Linear Mech. **67**, 394–404 (2014)
29. Alijani, F., Amabili, M., Balasubramanian, P., Carra, S., Ferrari, G., Garziera, R.: Damping for large-amplitude vibrations of plates and curved panels, part 1: modeling and experiments. Int. J. Non-Linear Mech. **85**, 23–40 (2016)
30. Amabili, M., Alijani, F., Delannoy, J.: Damping for large-amplitude vibrations of plates and curved panels, part 2: identification and comparisons. Int. J. Non-Linear Mech. **85**, 226–240 (2016)
31. Guo, X.: Shape memory alloy applications on control of thermal buckling, panel flutter and random vibration of composite panels. Ph.D. Thesis, Old Dominion University, Norfolk, VA (May 2005)
32. Abdel-Motagaly, K., Guo, X., Duan, B., Mei, C.: Active control of nonlinear panel flutter under yawed supersonic flow. AIAA J. **43**(3), 671–680 (2005)
33. Javanshir, J., Farsadi, T., Yuceoglu, U.: Free vibrations of composite base plates stiffened by two adhesively bonded plate strips. J. Aircr. **49**(4), 1135–1152 (2012)
34. Javanshir, J., Farsadi, T., Yuceoglu, U.: Free flexural vibration response of integrally-stiffened and/or stepped-thickness composite plates or panels. Int. J. Acoust. Vib. **19**(2), 114–126 (2014)
35. Farsadi, T., Heydarnia, E., Amani, P.: Buckling behaviour of composite triangular plates. J. GEOMATE **2**(2 (Sl. No. 4)), 253–260 (2012)